

# In Situ XAS and XRD Studies on the Structural Evolution of Ammonium Paratungstate During Thermal Decomposition

Olga Kirilenko,<sup>[a]</sup> Frank Girgsdies,<sup>[a]</sup> Rolf E. Jentoft,<sup>[a]</sup> and Thorsten Ressler\*<sup>[a]</sup>

**Keywords:** In situ studies / X-ray absorption spectroscopy / X-ray diffraction / Tungsten / Oxidation / Decomposition / Structure–activity relationships / Heterogeneous catalysis

The bulk structural evolution during the decomposition of ammonium paratungstate (APT) under various oxidizing and reducing gases was elucidated by the complementary techniques, in situ XAS, in situ XRD, and TG/DSC, combined with mass spectrometry. In the temperature range from 300 to 650 K, the decomposition of APT proceeds nearly independently of the gas employed. At higher temperatures, an oxidizing gas results in the formation of crystalline triclinic  $\text{WO}_3$  as the majority phase at 773 K, while mildly reducing gases (propene, propene and oxygen, and helium) result in the formation of partially reduced and highly disordered tungsten bronzes. No further reduction is observed under propene or helium, and this indicates a strongly hindered oxygen mobility in the tungsten oxide lattice in the temperature range employed. The decomposition of APT under hydrogen results in the formation of  $\text{WO}_2$  and, eventually, tungsten me-

tal. During the thermal treatment of APT, major changes occur at ca. 500 K where a complete structural rearrangement takes place that results in the destruction of the polyoxotungstate ion of APT and the formation of a tungsten oxide bronze. The rather low temperature for the formation of a three-dimensional lattice compared to the thermal treatment of common polyoxomolybdate precursors indicates the lower stability of the precursor and intermediates as ligands are removed. For tungsten to act as a potential structural or electronic promoter in molybdenum oxide based catalysts, tungsten needs to be incorporated in regular molybdenum oxide structures already at a very early stage of the catalyst preparation.

(© Wiley-VCH Verlag GmbH & Co. KGaA, 69451 Weinheim, Germany, 2005)

## Introduction

Molybdenum oxide based catalysts are extensively employed for the partial oxidation of light alkanes and alkenes.<sup>[1]</sup> Binary molybdenum oxides have a limited catalytic applicability, mostly because of their tendency to readily transform into the less active molybdenum trioxide,  $\text{MoO}_3$ , under the reaction conditions. Thus, it would be desirable to stabilize the active nanostructure of the molybdenum oxides (e.g.  $\text{Mo}_5\text{O}_{14}$ -type structures<sup>[2]</sup>) with the substitution of some of the molybdenum by additional metal centers such as vanadium, niobium, or tungsten.

Mixed oxide catalysts are commonly prepared by chemically or physically mixing suitable catalyst precursors. In order to prepare and stabilize the appropriate molybdenum oxide phase, the behavior of the catalyst precursors during thermal treatment needs to be elucidated. Previously, we reported on the structural evolution of ammonium heptamolybdate (AHM)<sup>[3]</sup> and heteropolyoxomolybdates (HPOM)<sup>[4]</sup> during thermal activation.

Ammonium paratungstate  $[(\text{NH}_4)_{10}\text{H}_2\text{W}_{12}\text{O}_{42}\cdot 4\text{H}_2\text{O}]$  (APT) is a common precursor for the preparation of Mo/

W mixed oxides. Because they are less complex than the industrially employed catalysts, these oxides constitute suitable model systems to reveal structure–activity relationships of mixed oxides under the reaction conditions. Therefore, investigations of the decomposition of APT are required to identify and quantify tungsten oxide phases and their formation under various gases, and to reveal correlations between catalytic activity and the structural evolution of APT.

The thermal decomposition of APT has been investigated by numerous authors who employed a variety of methods.<sup>[5–18]</sup> Thermal analysis studies<sup>[14]</sup> combined with in situ Fourier transform infrared (FT-IR) spectroscopy<sup>[13]</sup> identified  $\text{WO}_3$  as the product of decomposition at temperatures above ca. 650 K. The mechanism for thermal decomposition of APT in air has been studied by X-ray diffraction, thermogravimetry, and IR and UV/Vis diffuse reflectance spectroscopy.<sup>[15]</sup> Ammonium tungsten bronze,  $(\text{NH}_4)_{0.33}\text{WO}_3$ , and hexagonal  $\text{WO}_3$  were identified in the calcination reaction of APT at 673 K for 2 h under static air. On heating up to 770 K, the tungsten bronze together with hexagonal  $\text{WO}_3$  transformed completely into triclinic tungsten trioxide.

In more detail, the decomposition of APT in air has been studied by in situ laser Raman spectroscopy (LRS) combined with thermal gravimetric analysis (TGA), differential

[a] Fritz-Haber-Institut of the MPG, Department of Inorganic Chemistry, Faradayweg 4–6, 14195 Berlin, Germany  
Fax: +49-30-8413-4405  
E-mail: resseller@fhi-berlin.mpg.de

thermal analysis (DTA), and X-ray diffraction (XRD).<sup>[16]</sup> It was found that the decomposition in air proceeds through three steps in the temperature ranges 300–473 K, 473–623 K and 623–773 K. The formation of  $\text{WO}_3$  was detected at temperatures above 623 K. Besides studies in air, the thermal decomposition of APT was also investigated under hydrogen.<sup>[17,18]</sup> In the temperature range 470–520 K, APT was found to decompose into  $(\text{NH}_4)_{0.33}\text{WO}_3$ . This compound is stable in the temperature range 520–840 K, and is reduced to a mixture of  $\text{WO}_2$  and tungsten metal at 870 K, while complete reduction to tungsten metal is achieved at about 1000 K. In total, although the decomposition of APT has been investigated before, several questions remain unanswered with regard to the sequence of formation of the intermediates, their characterization, and the dependence of the decomposition pathways on the reaction gases for catalytically relevant gas phases (e.g. propene, and propene and oxygen).

The catalytic properties of tungsten trioxide has been investigated in a variety of reactions.<sup>[19–25]</sup> The selective oxidation of propene to acrolein has been studied with two series of mixed molybdenum/tungsten oxide catalysts.<sup>[24,25]</sup> The first series of oxides exhibits the typical  $\text{WO}_3$ -type structure, which consists of corner-sharing  $\text{WO}_6$  units and the general formula  $\text{Mo}_x\text{W}_{1-x}\text{O}_3$  ( $x = 0.4–0.9$ ). The second series, with the general formula  $(\text{Mo}_x\text{W}_{1-x})_n\text{O}_{3n-1}$  ( $x = 0.4–0.9$ ;  $n = 8–14$ ), comprises crystallographic shear structures. Members of the latter series showed a higher conversion and selectivity than the corresponding members of the first series. Selectivity was found to decrease as the tungsten content increased and as the density of crystallographic shear planes decreased. In situ oxidation of the reduced molybdenum oxide series of catalysts  $(\text{Mo}_x\text{W}_{1-x})_n\text{O}_{3n-1}$  resulted in little change in selectivity but a significant decrease in conversion.

In this work, the decomposition of APT was studied with in situ X-ray diffraction (XRD) and in situ X-ray absorption spectroscopy (XAS) to reveal the influence of different treatment parameters on the decomposition process, and to provide a detailed analysis of the short- and long-range structure evolution during the treatments. The decomposition of APT was studied under various oxidative and reductive gases (oxygen, propene and oxygen, helium, propene, and hydrogen), and the structural changes detected are discussed and compared with the mechanism for the decomposition of common polyoxomolybdates.

## Results

### Characterization of Ammonium Paratungstate

The experimental X-ray diffraction pattern of APT is depicted in Figure 1 together with a simulated pattern and a schematic structural representation. The simulated pattern of APT was obtained by using the corresponding single-crystal structural data of APT [ $(\text{NH}_4)_{10}\text{H}_2\text{W}_{12}\text{O}_{42}\cdot 4\text{H}_2\text{O}$ , ICSD 15237,  $P2_1/n$ ,  $a = 15.08 \text{ \AA}$ ,  $b = 14.45 \text{ \AA}$ ,  $c = 11.00 \text{ \AA}$ ,  $\beta = 109.4^\circ$ ]. The refined lattice constants are  $a = 15.04 \text{ \AA}$ ,

$b = 14.46 \text{ \AA}$ ,  $c = 10.95 \text{ \AA}$ , and  $\beta = 109.1^\circ$ , which are in good agreement with the single-crystal data. The crystallite size calculated from XRD peak-broadening was about 600 nm. No further crystalline phases were detectable in the experimental pattern of APT. Figure 2 shows the experimental and theoretical  $\text{W}_{\text{LIII}}$ -edge EXAFS  $\text{FT}[\chi(k)\cdot k^3]$  of APT. The corresponding distances and Debye–Waller factors obtained from the XAFS refinement are given in Table 1. The model of the local structure around the W centers in the polyoxotungstate ion of APT is adequate to simulate the  $\text{W}_{\text{LIII}}$  EXAFS spectrum. The good agreement between the theoretical structural data (XRD, XAS, TG) and the experimental data confirms that the ammonium paratungstate tetrahydrate used does indeed correspond to  $(\text{NH}_4)_{10}\text{H}_2\text{W}_{12}\text{O}_{42}\cdot 4\text{H}_2\text{O}$  (ICSD 15237) and excludes the presence of major impurity phases, either crystalline or amorphous.

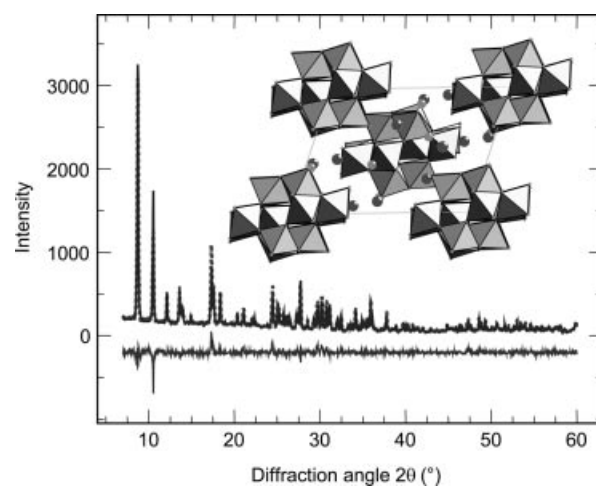


Figure 1. Experimental (dotted) and simulated (solid) X-ray diffraction pattern of ammonium paratungstate (APT), together with a schematic structural representation.

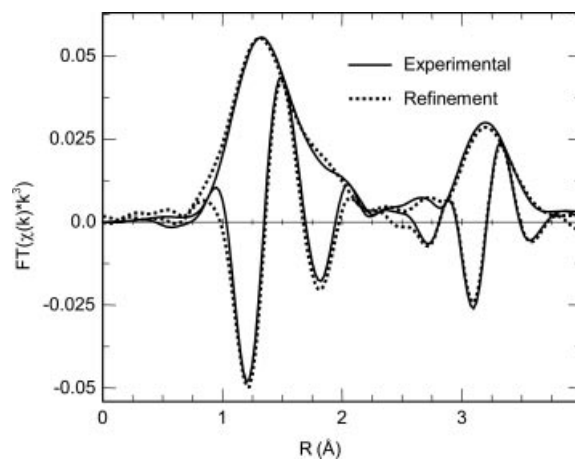


Figure 2. Experimental (dotted) and theoretical (solid)  $\text{W}_{\text{LIII}}$  XAFS  $\text{FT}[\chi(k)\cdot k^3]$  of ammonium paratungstate. Structural parameters are given in Table 1.

Table 1. Structural parameters [type of pairs and number ( $N$ ) of nearest neighbors at distance  $R$ ] obtained from a refinement of the ammonium paratungstate model structure (based on ICSD 15237) to the experimental XAFS functions  $\chi(k)$  of APT (Figure 2) at the  $W_{LIII}$  edge ( $N_{ind} = 23$ ,  $N_{free} = 14$ , 12 single scattering paths and 29 multiple scattering paths,  $R$  range 0.8–4.4 Å,  $k$  range 1.8–13.4 Å<sup>-1</sup>,  $E_0 = 7.6$  eV,  $S_0^2 = 0.9$ ).

Type	$N$	$R_{model}$ [Å]	$R$ [Å]	$\sigma^2$ [Å] <sup>2</sup>
W–O	1	1.72	1.70	0.0020
W–O	2	1.84	1.83	0.0021
W–O	1	1.92	1.96	0.0021
W–O	1	2.02	2.13	0.0022
W–O	1	2.30	2.26	0.0023
W–W	2	3.33	3.27	0.0035
W–W	2	3.70	3.67	0.0035
W–W	1	3.84	3.84	0.0036

### Thermal Decomposition of Ammonium Paratungstate (TG/DSC)

The evolution of the mass loss during thermogravimetric measurements of APT under various gases (helium, 5% hydrogen in helium, 20% oxygen in helium, 10% propene in helium, and 10% propene, and 10% oxygen in helium) is shown in Figure 3. The measurements were conducted at a heating rate of 6 K min<sup>-1</sup> and a total gas flow of 100 mL min<sup>-1</sup>. Additionally, the evolution of the MS signals for water ( $m/z = 18$ ) and ammonia ( $m/z = 15$ ) measured during the decomposition of APT under 20% oxygen are depicted in Figure 3. The gas-phase product composition is nearly identical for decomposition under oxygen, helium and hydrogen, even during the last step of the decomposition. In addition to the signals for water and ammonia, signals at  $m/z = 30$  and  $m/z = 44$  were also detected. These signals could be assigned to NO and N<sub>2</sub>O; however, the intensity of these signals follows the intensity of the signal for ammonia throughout the decomposition, and they may be artifacts formed by the mass spectrometer. Additionally, mass signals  $m/z = 30$  and  $m/z = 44$  were also detected during thermal decomposition of ammonium iodide (NH<sub>4</sub>I) in an inert gas, and this corroborates the assumption that these masses cannot be assigned unambiguously to the evolution of NO or NO<sub>2</sub> at particular reaction temperatures during the decomposition of APT.

In the temperature range 300–650 K, the evolution of the mass loss from APT during thermal decomposition is nearly independent of the gas employed. Four decomposition steps at 360, 470, 520, and 680 K can be distinguished in the TG and MS traces measured. The decomposition steps at 470, 520, and 680 K are accompanied by the evolution of water and ammonia, whereas for the decomposition steps at 360 K, only water is detectable in the gas phase. The weight loss after the first decomposition step at 360 K is 1.2% and corresponds to a loss of 2 equiv. of water of crystallization (1.1%). Apparently, the treatment under helium performed prior to the TG/DSC measurements to remove adsorbed water already reduced the number of equiv. of water of crystallization from the initial 4 to 2. The major mass loss of 8.8% at about 520 K is accompanied by the largest sig-

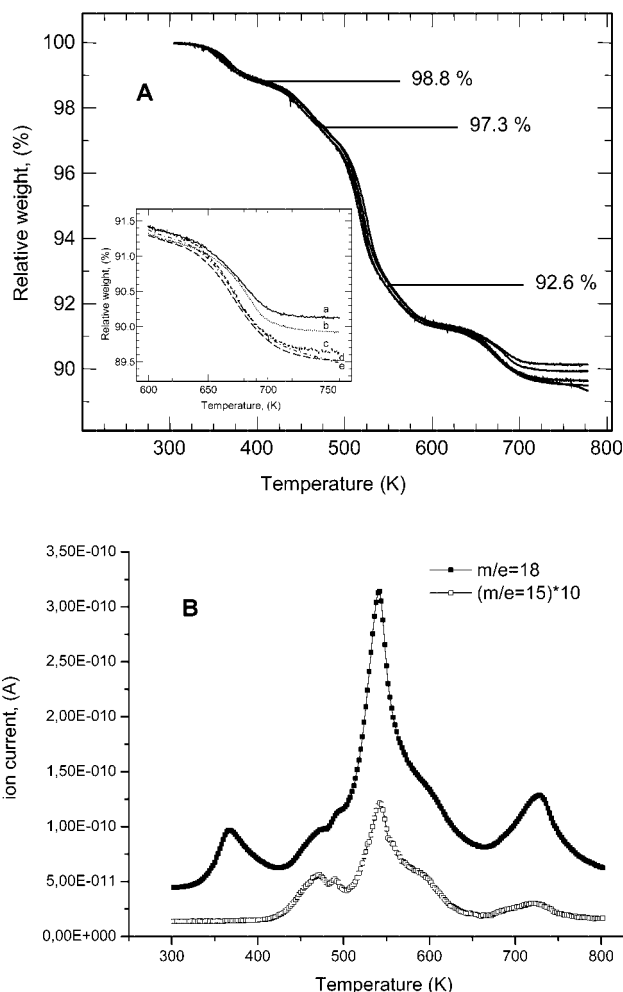


Figure 3. Evolution of relative weight during decomposition of ammonium paratungstate under (a) 20% oxygen in helium, (b) 10% propene and 10% oxygen in helium, (c) helium, (d) 10% propene in helium, and (e) 5% hydrogen in helium (flow rate 100 mL min<sup>-1</sup>, heating rate 6 K min<sup>-1</sup>), together with the MS signals for H<sub>2</sub>O ( $m/z = 18$ ) and NH<sub>3</sub> ( $m/z = 15$ ) measured for the decomposition of APT in 20% oxygen in helium.

nals in the water and ammonia MS traces. The total weight loss after the fourth decomposition step at 680 K depends on the gas used and is 9.9% under oxygen, 10.1% under propene and oxygen, 10.4% under helium, 10.5% under propene, and 10.8% under hydrogen. Because the decomposition under oxygen resulted in WO<sub>3</sub>, the other weight losses indicate the formation of partially reduced tungsten oxide species under reducing gases. Assuming that the initial material is identical, or alternatively, that the intermediates at 400 K are identical in composition, then the extent of reduction of the tungsten oxide at the end of the decomposition can be calculated. For the hydrogen-containing gas, this partial reduction results in an oxide formula of about WO<sub>2.85</sub>. The difference between a theoretical mass change when decomposing APT to WO<sub>3</sub> of 11.2% and the loss of 9.9% measured here during the decomposition under oxygen is accounted for by the above-mentioned loss of 2 equiv. of water of crystallization before the start of the TG experiments.

The differential scanning calorimetry traces measured during the decomposition of APT under various gases are depicted in Figure 4. Independent of the gas-phase composition, each of the first three mass losses shows one or more endothermic signals; the strongest endothermic signal accompanies the third decomposition step at about 520 K. The DSC measurements indicate an endothermic decomposition step at 700 K under reducing gases. However, a strong exothermic signal is observed at 700 K during the decomposition of APT under oxygen. Because the gas-phase products are nearly identical for both the oxygen and helium decomposition, the exothermic signal must be due either to a phase change, or to a reaction such as the re-oxidation of a somewhat reduced tungsten oxide, which would give no gas-phase products.

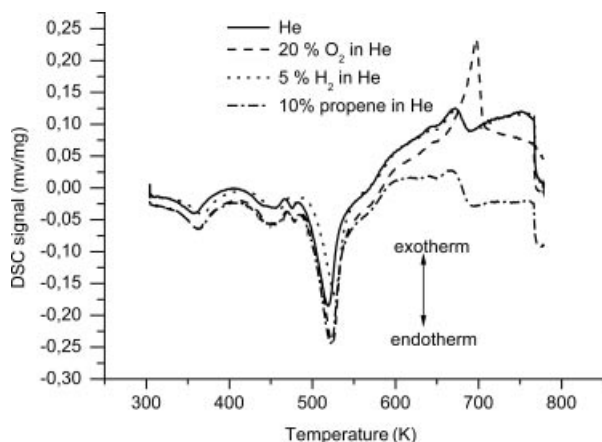


Figure 4. Comparison of the DSC signal measured during decomposition of ammonium paratungstate under helium (solid), 20% oxygen in helium (dashed), 5% hydrogen in helium (dotted), and 10% propene in helium (dash-dotted) (for the corresponding weight loss evolution see Figure 3).

### Thermal Decomposition of Ammonium Paratungstate (in Situ XRD and XAS)

#### Decomposition of APT under 20% Oxygen

The evolution of X-ray diffraction patterns measured during decomposition of APT under 20% oxygen in helium in the temperature range 300–770 K is depicted in Figure 5. Three major stages of the decomposition are indicated. The first series of patterns up to ca. 450 K corresponds to APT – a decreasing amount of water of crystallization accounts for the changes in peak intensities and phase composition observed. In the region from 450 K to about 620 K, a pronounced loss of crystallinity is visible from the XRD patterns. The few reflections detectable could not be assigned to any particular tungsten phase on the basis of the ICDD-PDF database. The last step in the structural evolution during decomposition of APT under oxygen at 620 K is accompanied by the occurrence of distinct XRD reflections, which can be assigned to triclinic  $\text{WO}_3$  as the major phase.

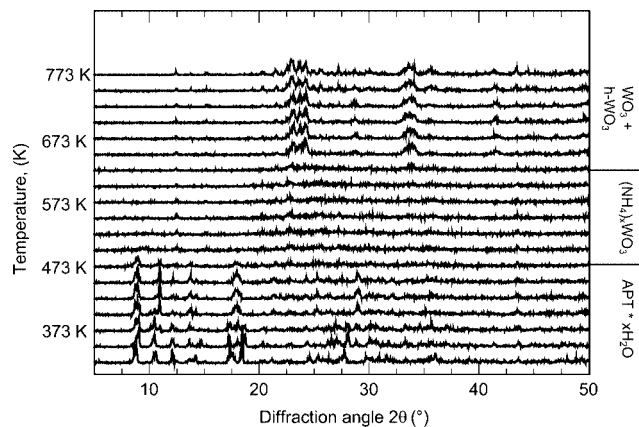


Figure 5. Evolution of X-ray diffraction patterns measured during decomposition of ammonium paratungstate under 20% oxygen in helium in the temperature range 300–770 K (effective heating rate  $0.1 \text{ K min}^{-1}$ , flow rate  $80 \text{ mL min}^{-1}$ ). Three major stages of the decomposition are indicated.

The  $\text{W}_{\text{LIII}}$ -edge XAFS  $\text{FT}[\chi(k) \cdot k^3]$  of APT measured during decomposition under 20% oxygen in helium in the temperature range 300–770 K are shown in Figure 6. Three temperature regions in the evolution of the local structure around the W centers can be distinguished. At 500 K, the initial APT spectrum exhibits changes, particularly, in the region between 2 and 4 Å (not phase-shift-corrected). The decreasing amplitude in this region indicates a significant loss of structural order. Conversely, the increasing amplitude of the first shell at ca. 1.5 Å indicates a decreasing degree of distortion in the first W–O coordination. At ca. 650 K, a decrease in the amplitude of the first shell and distinct changes in the region between 2 and 4 Å can be observed in the experimental  $\text{FT}[\chi(k) \cdot k^3]$ , which corresponds to the last step in the decomposition of APT.

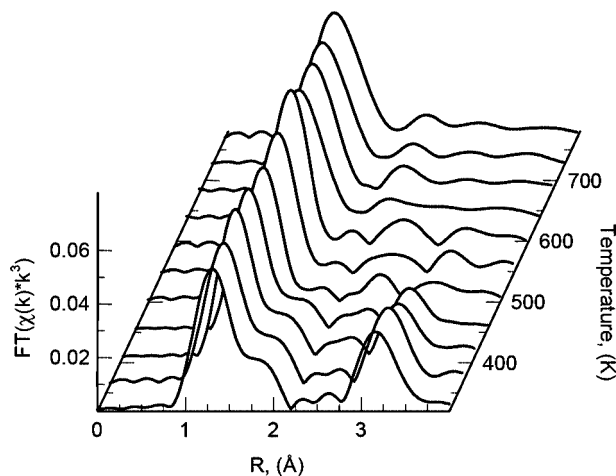


Figure 6. Evolution of  $\text{W}_{\text{LIII}}$ -edge XAFS  $\text{FT}[\chi(k) \cdot k^3]$  of ammonium paratungstate during decomposition under 20% oxygen in helium (heating rate  $5 \text{ K min}^{-1}$ , flow rate  $40 \text{ mL min}^{-1}$ ). Three principle regions can be distinguished: (300–500 K) APT, (500–650 K)  $(\text{NH}_4)_x\text{WO}_3$ , (650–770 K) triclinic  $\text{WO}_3$ .

### Decomposition of APT under Reducing Gases

The evolution of X-ray diffraction patterns measured during the decomposition of APT under 5% hydrogen in helium in the temperature range 300–770 K is depicted in Figure 7. Similar to the decomposition of APT under 20% oxygen, the first series of patterns up to about 450 K corresponds to APT with a decreasing amount of water of crystallization. In the region from 450 K to about 620 K, a complete loss of crystallinity is visible resulting in an X-ray-amorphous phase. At 620 K, the formation of highly disordered hexagonal and triclinic  $\text{WO}_3$  and tungsten oxide bronzes  $(\text{NH}_4)_x\text{WO}_3$  is observed. The  $\text{WO}_3$  formed exhibits a much lower crystallinity than that obtained during decomposition of APT under oxygen. Eventually, at 770 K under 5% hydrogen, the onset of the reduction of tungsten oxides to tungsten metal is detected in the XRD patterns. The evolution of the  $\text{W}_{\text{LIII}}$ -edge  $\text{FT}[\chi(k)\cdot k^3]$  measured during decomposition of APT under the reducing gases studied (i.e. propene, hydrogen, helium, propene and oxygen) is very similar to that of the decomposition under oxygen.

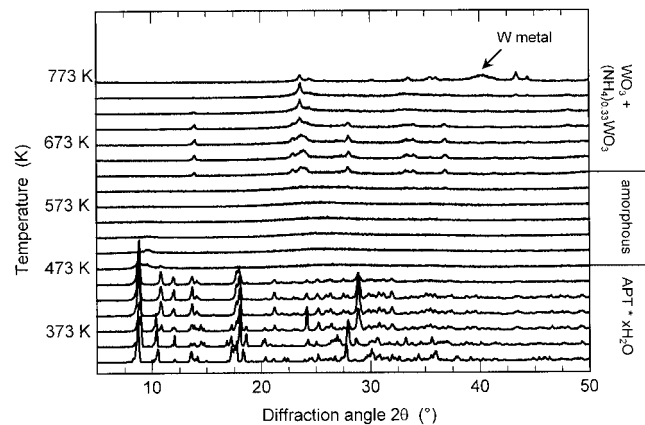


Figure 7. Evolution of X-ray diffraction patterns measured during decomposition of ammonium paratungstate under 5% hydrogen in helium in the temperature range 300–770 K (effective heating rate  $0.1 \text{ K min}^{-1}$ , flow rate  $80 \text{ mL min}^{-1}$ ). Three major stages of the decomposition are indicated.

### Decomposition of APT in Air (Static Conditions)

The evolution of X-ray diffraction patterns measured during the decomposition of APT in static air in the temperature range 300–770 K is shown in Figure 8. Similar to the decomposition of APT under oxygen, three major stages can be distinguished. The first series of patterns up to about 470 K corresponds to APT with a decreasing amount of crystal water. In the region from 470 K to about 550 K, the formation of an X-ray-amorphous phase is detected. Eventually, at 570 K, the formation of well-ordered and phase-pure triclinic  $\text{WO}_3$  is observed. The temperature range over which no crystalline phase is detected is smaller in static air than under flowing oxygen and hydrogen, and an increased stability of APT in the temperature region below 470 K and an accelerated formation of crystalline  $\text{WO}_3$  at 570 K already are observed. The onset temperature for

the decomposition of APT to the amorphous phase is increased by about 25 K, while the formation temperature of  $\text{WO}_3$  is lowered by about 25 K.

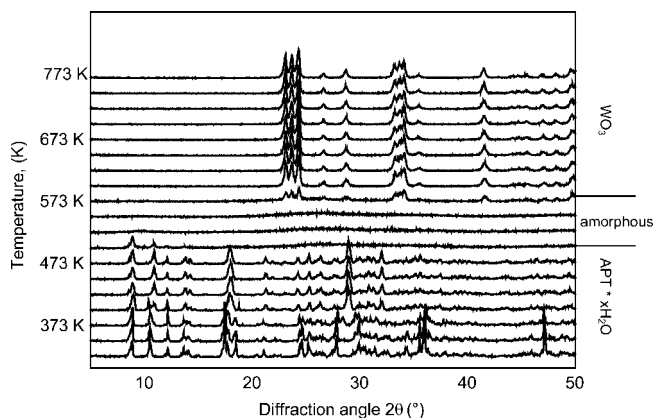


Figure 8. Evolution of X-ray diffraction patterns measured during decomposition of ammonium paratungstate in static air in the temperature range 300–770 K (effective heating rate  $0.1 \text{ K min}^{-1}$ , flow rate  $80 \text{ mL min}^{-1}$ ). Three major stages of the decomposition are indicated.

### Characterization of the Decomposition Intermediates and Products

The XRD pattern of the crystalline product of the decomposition of APT under 20% oxygen in helium can be simulated very well by a mixture of hexagonal and triclinic  $\text{WO}_3$  (Figure 9). A Rietveld refinement of the corresponding model structures to the experimental pattern resulted in a phase composition of ca. 90% triclinic  $\text{WO}_3$  and ca. 10% hexagonal  $\text{WO}_3$ , with crystallite sizes of 60 nm and 120 nm, respectively, and lattice constants that are in good agree-

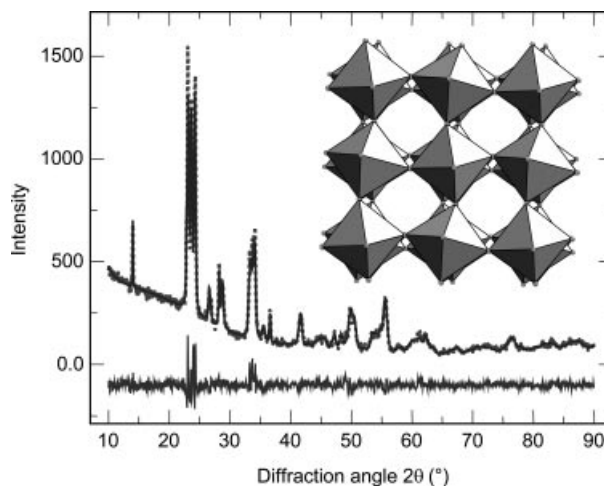


Figure 9. Experimental (dotted) and simulated (solid) X-ray diffraction pattern of the product of the decomposition of ammonium paratungstate under 20% oxygen in helium (300–770 K), together with a schematic structural representation of the corresponding triclinic  $\text{WO}_3$  phase.

ment with the single-crystal data [triclinic  $\text{WO}_3$  (ICSD 1620,  $a = 7.31 \text{ \AA}$ ,  $b = 7.52 \text{ \AA}$ ,  $c = 7.68 \text{ \AA}$ ,  $\alpha = 88.8^\circ$ ,  $\beta = \gamma = 90.9^\circ$ )  $a = 7.34 \text{ \AA}$ ,  $b = 7.53 \text{ \AA}$ ,  $c = 7.69 \text{ \AA}$ ,  $\alpha = 89.6^\circ$ ,  $\beta = \gamma = 90.5^\circ$ ]. A schematic representation of the structure of triclinic  $\text{WO}_3$  is depicted in Figure 9. The nearest-neighbor distances in triclinic  $\text{WO}_3$  are given in Table 2. The structure is related to the  $\text{ReO}_3$  structure and consists of edge-sharing  $\text{WO}_6$  units with W–O distances ranging from 1.8 to 2.2  $\text{ \AA}$ . In comparison with the  $\text{ReO}_3$  structure, the  $\text{WO}_6$  units in triclinic  $\text{WO}_3$  are strongly tilted with respect to each other resulting in a triclinic unit cell.

Table 2. Structural parameters [type of pairs and number ( $N$ ) of nearest neighbors at distance  $R$ ] obtained from a refinement of a triclinic  $\text{WO}_3$  model structure (based on ICSD 1620) and a hexagonal  $(\text{NH}_4)_{0.25}\text{WO}_3$  model structure (ICSD 23537) to the experimental XAFS functions  $\chi(k)$  of the product (at 300 K; Figure 10B) and of an intermediate (at 545 K; Figure 10A) of the decomposition of APT under oxygen at the  $\text{WL}_{\text{III}}$  edge ( $N_{\text{ind}} = 28$ ,  $N_{\text{free}} = 16$ , 12 single-scattering paths and 29-multiple scattering paths,  $R$  range 0.8–4.2  $\text{ \AA}$ ,  $k$  range 1.7–13.1  $\text{ \AA}^{-1}$ ,  $E_0 = 6.2 \text{ eV}$ ,  $S_0^2 = 0.9$ ).

Type	$N$	$\text{WO}_3$			$N$	$(\text{NH}_4)_{0.25}\text{WO}_3$		
		Model $R$ [ $\text{ \AA}$ ]	Product (300 K) $R$ [ $\text{ \AA}$ ]	$\sigma^2$ [ $\text{ \AA}^2$ ]		Model $R$ [ $\text{ \AA}$ ]	Intermediate (545 K) $R$ [ $\text{ \AA}$ ]	$\sigma^2$ [ $\text{ \AA}^2$ ]
W–O	3	1.78	1.78	0.0014	2	1.88	1.75	0.0040
W–O	1	1.95	1.95	0.0015	2	1.89	1.90	0.0041
W–O	1	2.06	2.07	0.0015	2	1.96	2.13	0.0042
W–O	1	2.21	2.19	0.0016	–	–	–	–
W–W	2	3.71	3.71	0.0060	4	3.70	3.65	0.0084
W–W	3	3.80	3.81	0.0060	2	3.78	3.74	0.0084
W–W	1	3.86	3.90	0.0060	–	–	–	–

A detailed XAFS analysis of the APT decomposition product under oxygen and of a representative intermediate of the decomposition from the amorphous region in the XRD series was performed to elucidate the local structure around the W centers in the two stages of decomposition. The experimental and theoretical  $\text{WL}_{\text{III}}$   $\text{FT}[\chi(k) \cdot k^3]$  of the intermediate of the thermal decomposition of APT at 523 K and of  $\text{WO}_3$  as the product of the decomposition at 773 K are depicted in Figure 10, A and B, respectively. The corresponding structural parameters are given in Table 2. It can be seen that the local structure around the W centers in the product  $\text{WO}_3$  is in good agreement with that in the triclinic  $\text{WO}_3$  model structure. Similarly, the local structure around the W center in the intermediate of the decomposition at 523 K can also be simulated by the triclinic  $\text{WO}_3$  model structure. However, characteristic deviation in the first W–O distances (i.e. absence of neighbors at 2.2  $\text{ \AA}$ ) indicates a higher degree of regularity in the  $\text{WO}_6$  units of the intermediate phase relative to those of triclinic  $\text{WO}_3$ . Moreover, the W–W distances obtained are slightly smaller than those determined for triclinic  $\text{WO}_3$ . It emerges that the local structure around the W centers in the intermediate phase at 523 K can be better explained by assuming a hexagonal tungsten bronze such as  $(\text{NH}_4)_{0.25}\text{WO}_3$  (ICSD 23537). A schematic structural representation of  $(\text{NH}_4)_{0.25}\text{WO}_3$  is depicted in Figure 11.

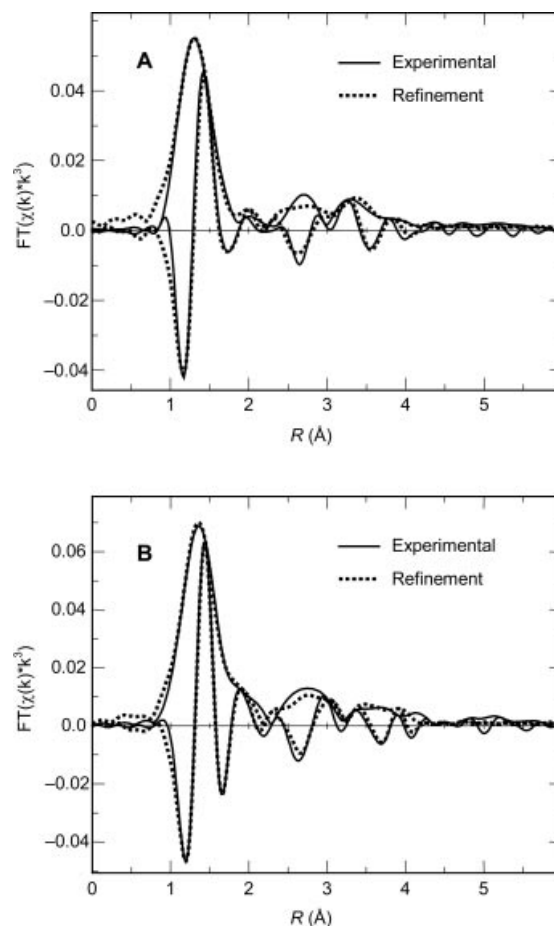


Figure 10. Experimental (dotted) and theoretical (solid)  $\text{WL}_{\text{III}}$  XAFS  $\text{FT}[\chi(k) \cdot k^3]$  of the intermediate of the thermal decomposition of ammonium paratungstate at 523 K (A) and of  $\text{WO}_3$  as the product of the decomposition at 773 K (B) measured at 300 K. The corresponding structural parameters are given in Table 2.

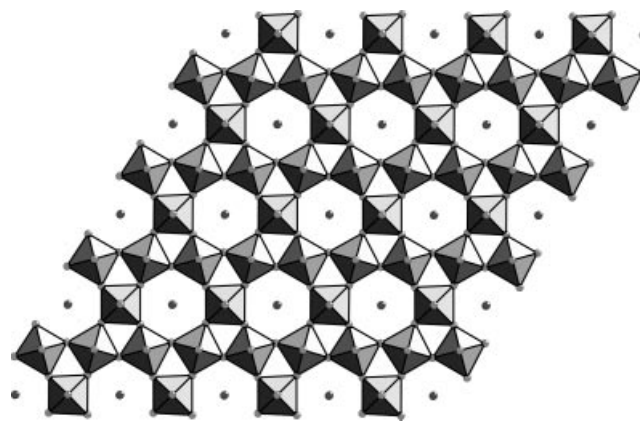


Figure 11. Schematic structural representation of hexagonal  $(\text{NH}_4)_{0.25}\text{WO}_3$  (ICSD 23537).

## Discussion

### Thermal Decomposition of Ammonium Paratungstate

The thermal analysis data shown in Figures 3 and 4 for the decomposition of APT under the various gases em-

ployed indicate that up to a temperature of ca. 650 K, the decomposition proceeds largely independently of the gas. This is corroborated by the XRD data presented in Figures 5, 7, and 8, which exhibit a series of patterns corresponding to a loss of water of crystallization up to 470 K, and transformation into a poorly crystalline or amorphous phase that persists up to ca. 650 K. At temperatures above 650 K, the product of decomposition depends on the gas-phase composition. This holds for both the phase composition and the crystallinity of the products obtained.

While under oxidizing gases triclinic  $\text{WO}_3$  is formed as the majority phase,<sup>[14,18]</sup> the decomposition under reducing gases results in the formation of partially reduced tungsten bronzes.<sup>[16]</sup> However, reduction of  $\text{WO}_{3-x}$  formed at 650 K under reducing gases (i.e. helium, propene, and hydrogen) to  $\text{WO}_2$  or tungsten metal is detected during the decomposition of APT under hydrogen only.<sup>[17,26–28]</sup> Apparently, propene is not capable of further reducing  $\text{WO}_3$  in the temperature range employed. This difference between the reducing powers of hydrogen and propene has already been observed for the reduction of  $\text{MoO}_3$  under propene and hydrogen.<sup>[29]</sup> While hydrogen is capable of entering the lattice of  $\text{MoO}_3$  and  $\text{WO}_3$ , reduction of the oxide by propene requires the facilitated diffusion of oxygen to the surface to react with the propene molecules adsorbed at the surface. On the one hand, this is the case for the reduction of  $\text{MoO}_3$  under propene and helium, where oxygen can readily diffuse in the layer structure of orthorhombic  $\text{MoO}_3$ . On the other hand, diffusion of oxygen appears to be considerably hindered in the  $\text{ReO}_3$ -type structure of  $\text{WO}_3$ . Thus, no lattice oxygen is made available at the surface of the  $\text{WO}_{3-x}$  crystallites formed in the decomposition of APT, and no significant oxidation of propene by lattice oxygen with the corresponding reduction of the  $\text{WO}_3$  lattice occurs.

The major mass loss (Figure 3) and thermal DSC event (Figure 4), together with the major structural changes (e.g. Figure 5) during the decomposition of APT proceeds at ca. 520 K. The amorphous or poorly crystalline phase detected by XRD at temperatures above 500 K can be identified by XAS to correspond to a 3D network structure similar to that of triclinic  $\text{WO}_3$ . While the local coordination of tungsten by the nearest-neighbor oxygen atoms in the intermediate phase at 500 K exhibits a characteristic distortion very similar to that of triclinic  $\text{WO}_3$  (and different from that of hexagonal  $\text{WO}_3$ ), the medium-range order appears to be more similar to that of a hexagonal  $\text{WO}_3$  structure,  $(\text{NH}_4)_{0.25}\text{WO}_3$ . A schematic representation of  $(\text{NH}_4)_{0.25}\text{WO}_3$  is depicted in Figure 11. The rather short W–W distances found in the local structure around the W center in the intermediate at ca. 500 K is characteristic for this hexagonal tungsten oxide. Hence, the major decomposition stage observed at ca. 500 K corresponds to a complete destruction of the polyoxo ions of APT, followed by a restructuring and formation of a three-dimensional network of corner-sharing  $\text{WO}_6$  units. During the decomposition in the temperature range 470–650 K prior to the formation of triclinic  $\text{WO}_3$ , the evolution of  $\text{FT}[\chi(k)\cdot k^3]$  shows that the distortion in the first oxygen coordination sphere decreases re-

sulting in more regular  $\text{WO}_6$  units similar to those characteristic of tungsten bronzes. With increasing temperature, the last decomposition stage and formation of triclinic  $\text{WO}_3$  at ca. 650 K results in an increased distortion of the  $\text{WO}_6$  units characteristic of triclinic  $\text{WO}_3$ .

### Decomposition of APT under Partial Oxidation Reaction Conditions

During the decomposition of APT under propene, and propene and oxygen no significant amounts of oxidation products of propene (i.e. acrolein or carbon dioxide) are detected in the gas phase. As mentioned above, no reduction of  $\text{WO}_3$  by propene is detected, indicating no availability of lattice oxygen for propene oxidation. The absence of propene oxidation activity in the temperature range studied is in agreement with a generalized mechanism of propene oxidation, which requires a certain weakening of the metal–oxygen bonds to ensure the presence of characteristic surface defects required for the activation of gas-phase oxygen and propene and the availability of oxygen to the gas-phase reactants.<sup>[30,31]</sup> The invariance of the  $\text{WO}_3$  structure under propene, and propene and oxygen at temperatures above 600 K indicates that the W–O bonds in the more regular  $\text{WO}_6$  building units of  $\text{WO}_3$ , relative to the highly distorted  $\text{MoO}_6$  building units of  $\alpha\text{-MoO}_3$ , are less susceptible of forming non-oxygen-terminated catalytically active surface sites. Conversely, treatment of  $\text{MoO}_3$  under propene and oxygen clearly shows that the onset of catalytic activity at ca. 600 K is correlated to the mobility of lattice oxygen at this temperature. The latter is evident from the onset of reduction of  $\text{MoO}_3$  under propene at the same temperature. In contrast with the characteristic layer structure of orthorhombic  $\text{MoO}_3$ , which is capable of accommodating oxygen vacancies by the formation of crystallographic shear defects, the corner-sharing octahedrons in the triclinic  $\text{WO}_3$  structure are less flexible, energetically more stable and are thus not capable of permitting an increased amount of oxygen vacancies in the tungsten oxide lattice. Under the decomposition conditions investigated, which encompass those used for the calcination of catalyst precursors in the literature, no catalytically active tungsten oxide bronzes or tungsten oxide shear-structures are obtained. The rather stable  $\text{ReO}_3$ -like three-dimensional tungsten oxides that already form at temperatures as low as 500 K exhibit no sufficient oxygen mobility and, hence, no partial oxidation activity in the temperature range employed.

### Comparison of the Decomposition of APT and Polyoxomolybdates

In previous works, we reported on the characteristic evolution of phases during the decomposition of ammonium heptamolybdate (AHM)<sup>[3]</sup> and heteropolyoxomolybdate (HPOM)<sup>[4]</sup> under various reaction gases. In Figure 12 the schematic pathway for the decomposition of APT is compared to those determined for the decomposition of AHM

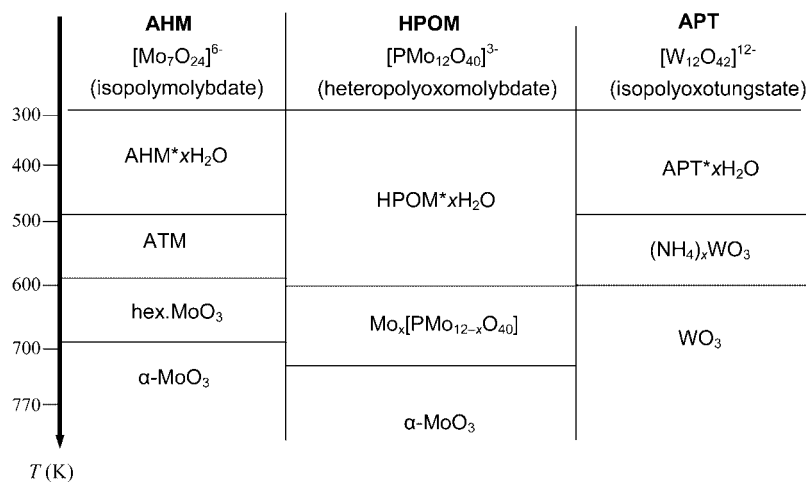


Figure 12. Schematic representation of the structural evolution during decomposition of ammonium heptamolybdate (AHM), a Keggin-type heteropolyoxo molybdate ([PMo<sub>12</sub>O<sub>40</sub>]<sup>3-</sup>), and ammonium paratungstate [(NH<sub>4</sub>)<sub>10</sub>H<sub>2</sub>W<sub>12</sub>O<sub>42</sub>·4H<sub>2</sub>O] under 20% oxygen in helium in the temperature range 300–773 K.).

and HPOM under oxygen. In all three cases, decomposition starts with the loss of water of crystallization, present in varying amounts in the three materials. The decomposition of the relatively small Anderson-type polyoxomolybdate ions of AHM proceeds according to a series of polycondensation steps that result in an increasing dimensionality of the structure of the decomposition intermediates.<sup>[3]</sup> The X-ray-amorphous phase that forms at ca. 500 K during the decomposition of AHM under flowing reactants could be identified as ammonium tetramolybdate possessing a 1D chain structure. A three-dimensional lattice structure (hexagonal MoO<sub>3</sub>) forms at ca. 600 K and is eventually transformed into orthorhombic MoO<sub>3</sub> at ca. 700 K. Evidently, the thermal decomposition of both APT and AHM proceeds through the formation of an ammonium- and water-containing hexagonal phase, which eventually decomposes into mainly triclinic WO<sub>3</sub> and orthorhombic MoO<sub>3</sub>, respectively. In contrast to the decomposition of APT, the products obtained from the decomposition of AHM depend strongly on the gas employed.<sup>[3]</sup>

Heteropolyoxomolybdates of the Keggin type, [PMo<sub>12</sub>O<sub>40</sub>]<sup>3-</sup>, exhibit a significantly increased stability compared to APT, with a similar stoichiometry. Partial decomposition and reduction of the Keggin ion starts at about 600 K, which coincides with the formation of a three-dimensional lattice during decomposition of AHM. At 600 K, the HPOM forms a lacunary Keggin ion with one molybdenum center on an extra-Keggin framework position. This arrangement is stable to about 700 K where a complete structural rearrangement and formation of α-MoO<sub>3</sub> is detected. While the extra-Keggin Mo center certainly acts as the first step towards “condensation” of the Keggin ions and formation of the extended MoO<sub>3</sub> structure, no further well-defined intermediates with an increasing degree of condensation are observed. Because the decomposition of HPOM results eventually in the formation of MoO<sub>3</sub> at temperatures above 700 K, the final product composition at 773 K is strongly dependent on the gas used (i.e. MoO<sub>3</sub>

under oxidizing gases, MoO<sub>2</sub> under moderately reducing gases, and Mo metal under hydrogen). Thus, two effects result in a pronounced stability of the Keggin-type HPOM relative to APT. First, the stability of the three-dimensional network of edge-sharing WO<sub>6</sub> units in WO<sub>3</sub> favors the decomposition of polyoxotungstate and the formation of WO<sub>3</sub>. Second, the Keggin ions of heteropolyoxomolybdates are considerably stabilized by the phosphorus heteroatom. With respect to the preparation of tungsten-containing, mixed-metal oxide, the differences in the decomposition schemes revealed for ammonium paratungstate relative to other common catalyst precursors such as ammonium heptamolybdate and heteropolyoxomolybdates indicate certain prerequisites for suitable preparation routes. Because of the low formation temperature of a stable 3D lattice structure during decomposition of APT, precursor mixtures with APT as a separate phase will most likely result in oxide mixtures containing catalytically less interesting triclinic or hexagonal tungsten oxides. Hence, in order to use the structure-promoting and stabilizing effect of the W centers in mixed molybdenum oxide catalysts, tungsten has to be incorporated into the Mo precursors to ensure the presence of W in the final catalyst.

## Conclusions

The bulk structural evolution during the decomposition of APT under various oxidizing and reducing gases was elucidated by the complementary techniques in situ XAS, in situ XRD, and TG/DSC combined with mass spectrometry. In the temperature range 300–650 K, the decomposition of APT proceeds nearly independently of the gas employed. Oxidizing gases result in the formation of crystalline triclinic WO<sub>3</sub> as the majority phase at 773 K, while mildly reducing gases (propene, propene and oxygen, and helium) result in the formation of partially reduced and highly disordered tungsten bronzes. No further reduction is observed

under propene or helium, indicating strongly hindered oxygen mobility in the tungsten oxide lattice in the temperature range employed. Because of the particular reducing capabilities of hydrogen (i.e. incorporation in the lattice and formation of bronzes), the decomposition of APT under hydrogen results in the formation of  $\text{WO}_2$  and, eventually, tungsten metal.

During the thermal treatment of APT major changes occur at ca. 520 K where a complete structural rearrangement takes place which results in the destruction of the polyoxotungstate ion of APT and the formation of a tungsten oxide bronze. This bronze already exhibits a three-dimensional structure consisting of corner-shared  $\text{WO}_6$  units with a local structure around the W centers similar to that in triclinic  $\text{WO}_3$ . The rather low temperature for the formation of a three-dimensional lattice relative to the thermal treatment of common polyoxomolybdate precursors indicates the particular structural stability of the arrangement of corner-sharing  $\text{WO}_6$  units in  $\text{WO}_3$  and tungsten oxide bronzes. For tungsten to act as a potential structural or electronic promoter in molybdenum oxide based catalysts, tungsten needs to be incorporated in regular molybdenum oxide structures already at a very early stage of the catalyst preparation instead of employing paratungstate-containing phase mixtures.

## Experimental Section

**Ammonium Paratungstate Tetrahydrate,  $(\text{NH}_4)_{10}\text{H}_2\text{W}_{12}\text{O}_{42}\cdot 4\text{H}_2\text{O}$ :** Ammonium paratungstate tetrahydrate [APT,  $(\text{NH}_4)_{10}\text{H}_2\text{W}_{12}\text{O}_{42}\cdot 4\text{H}_2\text{O}$ ] was used as purchased (Osram). For the investigations described here, a sieved fraction with particles in the size range 100–200  $\mu\text{m}$  was employed (Figure 13).

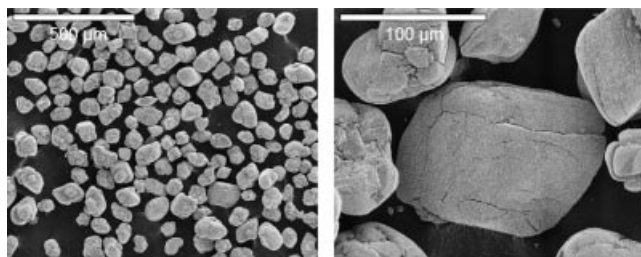


Figure 13. Scanning electron micrographs of a sieved fraction of as-purchased ammonium paratungstate [ $(\text{NH}_4)_{10}\text{H}_2\text{W}_{12}\text{O}_{42}\cdot 4\text{H}_2\text{O}$ ] with particles in the size range 100–200  $\mu\text{m}$ .

**X-ray Diffraction (XRD):** In situ XRD studies were performed with a STOE Bragg–Brentano diffractometer (Ge secondary monochromator,  $\text{Cu-K}\alpha$  radiation) equipped with a Bühler HDK S1 high-temperature cell. The product composition in the gas phase was continuously monitored by using a mass spectrometer in a multiple ion detection mode (Pfeiffer QMS 200). XRD measurements were conducted in the temperature range 323–773 K with an effective heating rate of 0.1  $\text{K min}^{-1}$ . Diffraction patterns were recorded every 25 K in a  $2\theta$  range of 5–50°. Analysis of experimental diffraction patterns was performed by using the software TOPAS (Bruker AXS) Version 2.1. Crystallite sizes were estimated by using the Scherrer equation. The ICDD-PDF (International center for dif-

fraction data) database and the ICSD (Inorganic crystal structure database) were used for phase analysis and structure refinement.

**X-ray Absorption Spectroscopy (XAS):** Transmission X-ray absorption spectra were measured in situ with the sample pellet in a flow reactor under a controlled reactant gas.<sup>[32]</sup> In situ XAS experiments were performed at the  $\text{W}_{\text{LIII}}$  edge (10.204 keV) (Hamburger Synchrotronstrahlungslabor, HASYLAB, beamline X1), by using an Si (311) double crystal monochromator. Temperature-programmed decomposition of APT was conducted at temperatures between 293 and 773 K under helium, 5% hydrogen in helium, 20% oxygen in helium, 10% propene in helium, and 10% propene and 10% oxygen in helium. For the in situ XAS measurements, 4 mg of APT was mixed with 30 mg of boron nitride and pressed into pellets of 5 mm in diameter (edge jump  $\Delta\mu_x \approx 1.5$  at the  $\text{W}_{\text{LIII}}$  edge). The gas-phase composition was continuously monitored by using a mass spectrometer in a multiple ion detection mode (Omnistar, Pfeiffer). Data analysis of XAFS spectra was performed with the software WinXAS 3.0.<sup>[33]</sup> The spectra were energy-calibrated with respect to a tungsten metal foil reference spectrum. For background subtraction and normalization, first-order polynomials were refined to the pre-edge and EXAFS region. Spectra were converted to  $k$  space using an  $E_0$  defined as the first inflection point in the  $\text{W}_{\text{LIII}}$  edge. Atomic absorption,  $\mu_o$ , fitting was performed by using a cubic spline with 7 knots to minimize peaks at low  $R$  values ( $<1 \text{ \AA}$ ) in the Fourier-transformed EXAFS  $\chi(k)$ . The pseudo radial distribution function  $\text{FT}[\chi(k)\cdot k^3]$  was calculated by Fourier transforming the  $k^3$ -weighted experimental  $\chi(k)$  function, multiplied by a Bessel window, into the  $R$  space. EXAFS data analysis was performed by using theoretical backscattering phases and amplitudes calculated with the ab initio multiple-scattering code FEFF7.<sup>[34]</sup> Single-scattering and multiple-scattering paths in monoclinic APT, hexagonal  $(\text{NH}_4)_{0.25}\text{WO}_3$  (intermediate), and triclinic  $\text{WO}_3$  (decomposition product) were calculated up to 6.0  $\text{\AA}$  with a lower limit of 8.0% in amplitude with respect to the strongest backscattering path. EXAFS refinements were performed in  $R$  space simultaneously to magnitude and imaginary part of a Fourier transformed  $k^3$ -weighted and  $k^1$ -weighted experimental  $\chi(k)$  by using the standard EXAFS formula.<sup>[34]</sup> Structural parameters that are determined by a least-squares EXAFS refinement of a model structure to the experimental spectra are (i) one overall  $E_0$  shift, (ii) Debye–Waller factors for single-scattering paths, and (iii) distances of single-scattering paths. Coordination numbers (CN) and  $S_0^2$  were kept constant in the refinement.

**Thermal Analysis (TG and DSC):** Thermal analysis [thermogravimetry (TG) and differential scanning calorimetry (DSC)] was performed with a Netzsch STA 449 C TG/DSC instrument combined with an Omnistar (Pfeiffer) mass spectrometer under pure helium, 5% hydrogen in helium, 20% oxygen in helium, 10% propene in helium, and 10% propene, and 10% oxygen in helium. Measurements were carried out at heating rates of 6  $\text{K min}^{-1}$ , and at a total flow of 100  $\text{mL min}^{-1}$ .

**Scanning Electron Microscopy:** Scanning electron microscopy (SEM) was conducted with an S 4000 FEG microscope (Hitachi). The acceleration voltage was set at 10 kV, the objective aperture was 30 mm, and the working distance was 10 mm.

## Acknowledgments

The Hamburger Synchrotronstrahlungslabor, HASYLAB, is acknowledged for providing beamtime for this work. G. Weinberg is acknowledged for conducting the SEM measurements. We thank B. Kniep, A. Szzybalski, E. Rödel, J. Osswald, and J. Wienold for

assistance at the beamline and for numerous valuable discussions. The authors are grateful to Prof. R. Schlögl for his continuous support.

- [1] A. Bielanski, J. Haber, *Oxygen in Catalysis*, Marcel Dekker, New York, **1991**.
- [2] S. Knobl, G. A. Zenkovets, G. N. Kryukova, O. Ovsitser, D. Niemeyer, R. Schlögl, G. Mestl, *J. Catal.* **2003**, *215*, 177–187.
- [3] J. Wienold, R. E. Jentoft, T. Ressler, *Eur. J. Inorg. Chem.* **2003**, 1058–1071.
- [4] J. Wienold, O. Timpe, T. Ressler, *Chem. Eur. J.* **2003**, *9*, 1–12.
- [5] E. Lassner, W. Schubert, *Thermochim. Acta* **2000**, *343*, 139–143.
- [6] B. Gerand, G. Nowogrocki, M. Figlarz, *J. Solid State Chem.* **1981**, *38*, 312–320.
- [7] M. F. Daniel, B. Desbat, J. C. Lassegues, B. Gerand, M. Figlarz, *J. Solid State Chem.* **1987**, *67*, 235–247.
- [8] John W. van Put., G. J. Witkamp, G. M. van Rosmalen, *Hydro-metallurgy* **1993**, 187–201.
- [9] Y. Zhu, A. Manthiram, *J. Solid State Chem.* **1994**, *110*, 187–189.
- [10] J. Pfeifer, E. Badaljan, P. Tekula-Buxbaum, T. Kovacs, O. Geszti, A. L. Toth, H.-J. Lunk, *J. Cryst. Growth* **1996**, *169*, 727–733.
- [11] N. E. Fouad, A. K. H. Nohman, M. J. Zaki, *Thermochim. Acta* **1994**, *239*, 137–145.
- [12] M. Boulouwa, G. Lucazeau, *J. Solid State Chem.* **2002**, *167*, 425–434.
- [13] C. Li, H. Zhang, K. L. Wang, Y. F. Miao, Q. Xin, *Appl. Spectrosc.* **1993**, *47*, 56–61.
- [14] I. K. Bhatnaga, D. K. Chakraba, A. B. Biswas, *Indian J. Chem.* **1972**, *10*, 1025–1028.
- [15] N. E. Fouad, A. K. H. Nohman, M. A. Mohamed., M. J. Zaki, *J. Anal. Appl. Pyrolysis* **2000**, *56*, 23–31.
- [16] X. S. Li, B. Z. Zhu, L. Wang, Y. F. Miao, Q. Xin, *Chin. Chem. Lett.* **1995**, *6*, 1085–1086.
- [17] N. E. Fouad, A. K. H. Nohman, *Thermochim. Acta* **2000**, *343*, 139–143.
- [18] J. Pfeifer, E. G. Badaljan, P. Tekula-Buxbaum, K. Vadasdi, *J. Solid State Chem.* **1993**, *105*, 588–594.
- [19] I. Rodriguez-Ramos, A. Guerro-Ruiz, N. Homs, R. de la Piscina, J. L. G. Fierro, *J. Mol. Catal.* **1995**, *95*, 147–156.
- [20] D. Hoegaets, B. Sels, D. Fos, F. Verpoort, P. Jacobs, *Catal. Today* **2000**, *60*, 209–218.
- [21] M. O'Keefe, *Fast Ion Transport in Solids – Solid State Batteries and Devices*, Elsevier, New York, **1973**, 233–247.
- [22] A. Cimino, F. S. Stone, *Adv. Catal.* **2002**, *47*, 141–306.
- [23] S. De Rossi, I. Igughi, M. Schiavello, R. J. D. Tilley, *Z. Phys. Chem. (Muenchen Ger.)* **1976**, *103*, 193–202.
- [24] J. Haber, J. Janas, M. Schiavello, R. J. D. Tilley, *J. Catal.* **1983**, *82*, 395–403.
- [25] S. Barber, J. Booth, D. R. Pyke, R. Reid, R. J. D. Tilley, *J. Catal.* **1982**, *77*, 180–191.
- [26] D. S. Venables, M. E. Brown, *Thermochim. Acta* **1996**, *285*, 361–382.
- [27] C. Bigey, L. Hilaire, G. Maire, *J. Catal.* **1999**, *184*, 406–420.
- [28] V. Logie, P. Wehrer, A. Katrib, G. Maire, *J. Catal.* **2000**, *189*, 438–448.
- [29] T. Ressler, R. E. Jentoft, J. Wienold, T. Neisius, *J. Catal.* **2002**, *210*, 67–83.
- [30] P. Mars, D. W. van Krevelen, *Chem. Ing. Sci.* **1954**, *3*, 41–52.
- [31] T. Ressler, J. Wienold, R. E. Jentoft, F. Girgsdies, *Eur. J. Inorg. Chem.* **2003**, 301–312.
- [32] T. Ressler, R. E. Jentoft, J. Wienold, M. M. Guenter, O. Timpe, *J. Phys. Chem. B* **2000**, *104*, 6360–6370.
- [33] T. Ressler, *J. Synchrotron Radiat.* **1998**, *5*, 118–122.
- [34] J. J. Rehr, C. H. Booth, F. Bridges, S. I. Zabinsky, *Phys. Rev. B* **1994**, *49*, 12347–12350.

Received: October 15, 2004